Defect Chemistry and Catalytic Activity of Nanosized Co_3O_4

M. Casas-Cabanas, G. Binotto, D. Larcher,* A. Lecup, V. Giordani, and J.-M. Tarascon

Laboratoire de Réactivité et Chimie des Solides, Université de Picardie Jules Verne, CNRS UMR6007, 33 rue Saint Leu 80039 Amiens, France

Received February 4, 2009. Revised Manuscript Received March 11, 2009

Nanometric cobalt oxide Co_3O_4 powders made of 4 nm isotropic particles, directly precipitated from Co^{2+} aqueous solutions under alkaline and oxidizing conditions, are found to exhibit abnormal X-ray diffraction intensities, mainly in (111) and (220) reflections, because of a significant amount of displaced Co atoms from ideal 8a and 16d positions to interstitial 48f and 16c sites. Upon heating, the Co/O stoichiometry is maintained and the delocalized atoms progressively migrate to stable positions through empty neighboring sites. Despite the presence of such defects, the order of reaction ($n \approx 1$) and the activation energy ($E_a \approx 60 \pm 5$ kJ/mol) versus the decomposition of diluted solutions of hydrogen peroxide solutions is found to be similar to bulk nonfaulted Co_3O_4 materials, but the intrinsic rate constants $k_{20\ °C}$ are found to be proportionally enhanced by both the defect and microstrains levels. Last, a careful selection of monolithic samples, so as to keep away the catalytic influence of the intercrystallites reactive grain-boundaries, has enabled us to precisely study and isolate the role of the structural characteristics on the catalytic activity of Co_3O_4 toward H_2O_2 decomposition. The catalytic activity of such divided oxides toward this reaction is also put forward as a fast selection tool for catalysts in Li-oxygen secondary cells.

Introduction

Co_3O_4 is an important technological material that is currently used in the hydrocracking process of crude fuels and in the treatment of waste gases.[1] More recently, it also became considered as a potential negative electrode material for lithium-ion batteries[2] and as a very promising catalytic agent for secondary Li/O_2 cells.[3] Indeed, this battery technology is based on the overall reaction of metallic Li with oxygen as follows: $2Li + O_2 \rightleftharpoons Li_2O_2$. In such a system, both electrodes are soaked in an organic electrolyte, and Li is oxidized into Li^+ at the anode side, whereas O_2 molecules are reduced into peroxide ions at the cathode side. These two half-reactions leads to the precipitation of Li_2O_2 ($2Li^+ + O_2^{2-} \rightleftharpoons Li_2O_2$) in the porous texture of the cathode electrode, and the reaction stops when the cathode porosity is totally filled with this precipitate. For sake of electronic conductivity, the porous cathode not only enlists divided carbon (electronic conductor additive) but also a catalyst material (e.g., MnO_2, Co_3O_4, etc.) whose major role is to minimize the activation energy involved in the back decomposition of the peroxide ($Li_2O_2 \rightarrow 2Li + O_2$) during the charge of the cell. It is needless to say that the efficiency of this catalyst is a mandatory aspect in view of lowering the cell polarization that is the main drawback of this technology.

All these applications are oriented toward the use of extremely small particles with high specific surface areas. Low-temperature "Chimie Douce" approaches constitute one of the most common strategies to prepare nanometric solids of controlled texture and morphology with therefore the risk/opportunity to precipitate kinetically promoted metastable phases,[4,5] including highly faulted materials whose imperfections will disappear by secondary growth and aging. These peculiarities related to synthesis might generate original and interesting properties that require a complete understanding of the type, concentration, and distribution of defects among the crystal.

We have recently reported a simple synthesis procedure of nanosize (4 nm) stoichiometric Co_3O_4 monolithic particles (Co_3O_4-AP) by direct precipitation from Co^{2+} aqueous solutions under highly alkaline and oxidizing conditions.[6] These nanometric domains are forming micrometric agglomerates exhibiting high porosity (~40%), very fine porous distribution centered at 4 nm, and no detectable porosity beyond 10 nm. During annealing of this precursor, the porous volume (i.e., porous surface) as well as its distribution drastically evolves, as detailed in ref 6. Whatever the porous initial characteristics of the powders, pristine or annealed, a few minutes of mortar/pestle hand-milling always results in a very large fragmentation of the agglomerates and in the creation of pores with much larger diameters, hence a more accessible surface.

Co_3O_4 ideally crystallizes in the spinel structure ($Fd\bar{3}m$) that can be described as an almost-perfect cubic close-packed arrangement of oxygen ions with cations distributed among

* Corresponding author. E-mail: dominique.larcher@u-picardie.fr.

(1) Grillo, F.; Natile, M. M.; Glisenti, A. *Appl. Catal., B* **2004**, *48* (4), 267.
(2) Poizot, P.; Laruelle, S.; Grugeon, S.; Dupont, L.; Tarascon, J. M. *Nature (London)* **2000**, *407*, 496.
(3) Debart, A.; Bao, J.; Armstrong, G.; Bruce, P. G. *J. Power Sources* **2007**, *174* (2), 1177.
(4) Livage, J.; Brec, R.; Catherine, Y.; Cot, L.; Figlarz, M.; Portier, J.; Rouxel, J.; Tournoux, M. *Ann. Chim.* **1989**, *14* (5−7), 353.
(5) Figlarz, M.; Gerand, B.; Dumont, B.; Delahaye-Vidal, A.; Portemer, F. *Phase Transitions* **1991**, *31* (1−4), 167.
(6) Binotto, G.; Larcher, D.; Prakash, A. S.; Urbina, R. H.; Hedge, M. S.; Tarascon, J. M. *Chem. Mater.* **2007**, *19* (12), 3032.

10.1021/cm900328g CCC: $40.75
Published on Web 04/16/2009

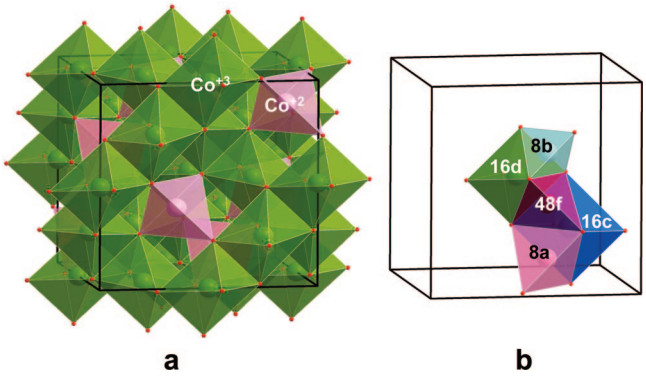

Figure 1. (a) Atomic structure of an ideal Co_3O_4 phase and (b) local environments of the different available crystallographic sites in this structure.

tetrahedral and octahedral sites. However, the characterization of our low-temperature precipitated powders (Co_3O_4-AP) revealed an abnormal intensity distribution in their X-ray diffraction patterns, as the relative intensities of the (111) and (220) reflections were inverted when compared to a normal spinel structure, indicating some kind of structural disorder.

In the ideal Co_3O_4 structure, the unit-cell contains 8 elemental cells in which one-eighth of the available tetrahedral sites (8a Wyckoff sites) are occupied by divalent cations and half of octahedral sites (16d Wyckoff sites) are occupied by trivalent cations. This $[Co^{+II}]_{8a}[Co^{+III}_2]_{16d}[O_4]_{32e}$ ideal arrangement corresponds to the so-called normal-spinel structure (Figure 1a). Other arrangements exist as the inverse-spinel structure, in which one-eighth of the tetrahedral sites and one-fourth of the octahedral sites are occupied by trivalent atoms while one-fourth of octahedral sites are occupied by divalent ones. In practice, most of the synthetic spinels adopt an intermediate state and the inversion parameter i is used to define the fraction of trivalent cations in the octahedral site, which is thus equal to the fraction of divalent cations in tetrahedral sites. Other types of disorder are reported in spinels, one being typically their tendency toward nonstoichiometry. For example, hausmanite (Mn_3O_4) tends to form oxygen-rich compounds ($Mn_{3-\delta}O_4$) resulting in cationic vacancies that compensate for the excess of Mn^{3+},[7] or magnetite (Fe_3O_4), for which it has been reported that both cation vacancies and interstitial cations contribute to the cationic diffusion properties as shown from oxygen activity measurements.[8] Even more complex situations have been described, as for $LiMn_2O_4$ thin films, in which two intergrown spinel components with configuration $[Li_{1-x-y}]_{8a,8b,48f}[Li_xMn_z\square_{2-x-z}]_{16c}[Li_yMn_{2-z}\square_{z-y}]_{16d}O_4$ would coexist.[9] In all cases, oxygen ions form a cubic face-centered arrangement although they are slightly displaced from the ideal 1/4 1/4 1/4 position, causing a dilatation of the anionic sub cell. The anionic parameter (u), which corresponds to their position in the unit cell (u,u,u), is used to give an idea of the compactness of the structure that turns out to very much depend on the cationic arrangement in the unit cell.

(7) Kaczmarek, J.; Wolska, E. *J. Solid State Chem.* **1993**, *103*, 387.
(8) Dieckmann, R. *Solid State Ionics* **1984**, *12*, 1.
(9) Thackeray, M. M. *J. Electrochem. Soc.* **1997**, *144* (5), L100.

Unlike other spinel structures, very few reliable data exist concerning the defect structure of stoichiometric Co_3O_4.[8] In this work, we present a thorough study of the defect chemistry of nanometric Co_3O_4 by means of Rietveld refinement of X-ray diffraction patterns. Different types of disorder have been considered to explain the origin of the intensity inversion of (111) and (220) reflections, and the independent influence of instrumental parameters, particle size, microstrains, and point defects on the broadening and intensity of the diffraction peaks has been ascertained. The evolution of such microstructural features upon annealing has also been scrutinized and a mechanism of defect migration with temperature by vacancy/interstitial recombination is presented from our experimental data.

The constant stoichiometry (i.e., metal oxidation state) between our pristine and annealed Co_3O_4 samples provides an unique opportunity to precisely test the intrinsic effect of the structural defects onto the catalytic activity of Co_3O_4, as the amount of defects can be modified without any change in their composition. This point will be addressed in the last part of this paper where preliminary results dealing with the catalytic decomposition of hydrogen peroxide solutions will be shown and compared. A link between the catalytic activity and the amounts of defects and strains will be proposed, and this test will be suggested as a selecting tool for catalysts in Li/O_2 cells.

Experimental Section

Powder Synthesis. Co_3O_4 samples were directly precipitated from a $Co(NO_3)_2 \cdot 6H_2O$ aqueous solution under highly alkaline and oxidizing conditions. In a typical preparation, 22 g of NaOH (Acros, 97%) is dissolved in 800 mL of deionized water in a five-necked flask and heated until boiling under reflux and constant stirring. Once boiling is reached, 16.3 g of $Na_2S_2O_8$ (68.7 mmol, Alfa Aesar, 98%) are dissolved into the solution. Next, 50 mL of a 0.69 M $Co(NO_3)_2 \cdot 6H_2O$ solution (10 g, Alfa Aesar, 97.7%) is added drop by drop and a black precipitate is instantaneously formed. The resulting suspension is aged at 95 °C for 1 h and then left to cool to room temperature and settle for 1 night. The black precipitate is then separated from the supernatant by centrifugation at 3000 rpm for 5 min, washed several times with a 2 mol L^{-1} HCl aqueous solution to remove byproduct such as β-CoOOH, washed with water to eliminate residual chlorine ions, and dried at 50 °C for 12 h. This as-prepared product will now be referred to as Co_3O_4-AP (for as-prepared). To study the evolution of the defect structure upon annealing, we heated equal amounts (ca. 200 mg) of Co_3O_4-AP under air (5°/min) at temperatures ranging from 150 to 800 °C and maintained the required temperature for 1 h. These samples are labeled as Co_3O_4 $_{T°C}$ (Co_3O_4 $_{150\ °C}$ to Co_3O_4 $_{800\ °C}$).

Powder Characterization. Thermogravimetric (TGA) data were collected under air (Mettler M3-TC11) in an open alumina crucible. All data were corrected for the variations of the buoyancy of the sample container itself.

The cobalt mean oxidation state has been measured by iodometric titration as detailed in ref 6.

Electron microscopy (TEM) images were obtained using a FEI Tecnai F20 S-Twin electron microscope operating at 200 kV. Specific surface areas and pore size/volume distribution were computed from the results of N_2 physisorption at 77 K (Micromeritics ASAP 2020) using the BET (Brunauer-Emmet-Teller)[10] and BJH (Barrett−Joyner−Halenda)[11] formalisms.

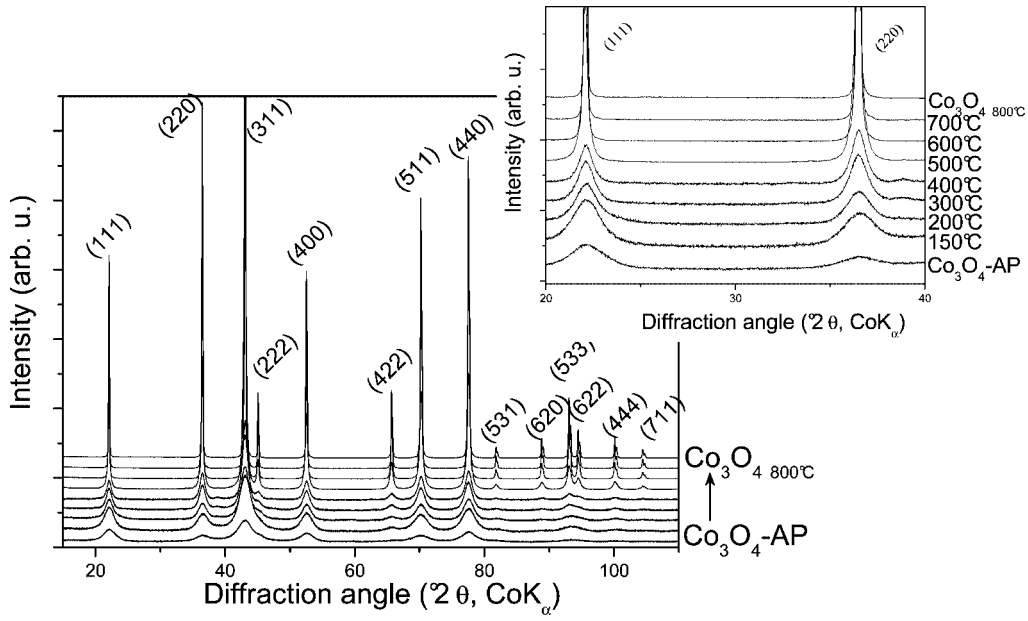

Figure 2. Evolution of the XRD diffraction patterns during the air-annealing of Co_3O_4-AP. The inset shows the evolution/inversion in intensity for the (111) and (220) reflections in the low-temperatures range.

X-ray diffraction (XRD) data were collected with a D8 Bruker-AXS diffractometer equipped with a Braun PSD (position sensitive detector) detector with Co Kα radiation ($\lambda_1 = 1.789190$ Å, $\lambda_2 = 1.793210$ Å) in Bragg−Brentano geometry in the range $2\theta = 10-110°$ with a step size of 0.012°. The instrumental resolution function (IRF) of the diffractometer was determined with an Al_2O_3 standard ($U = 0.003932$ deg^2, $V = -0.002207$ deg^2, $W = 0.002549$ deg^2).

Rietveld refinements were carried out with the FullProf program (Windows version, March 2007)[12] using the pseudo-Voigt profile function of Thompson, Cox and Hastings[13] taking as initial values those obtained in the diffraction study reported by Smith and Hobson.[14] Scale factor, zero point, cell dimensions, atomic coordinates, atomic occupations for cobalt atoms, and atomic displacement factors were refined. Background was fitted and refined by adjusting the height of preselected points for linear interpolation. The different angular dependence of the peak shape parameters on the scattering angle was used to model size and strain-broadening of the peaks, and the refined values were used to calculate the average size of the crystallites and the amount of microstrains (expressed as $\Delta d/d$, where d is the interplanar distance), according to the expressions of Scherrer[15] and Stokes and Wilson,[16] by previous correction of instrumental broadening.

Catalytic Tests. The catalytic activity of our samples is determined with respect to the decomposition of H_2O_2 in aqueous solution ($H_2O_2 \rightleftharpoons 1/2\ O_2 + H_2O$). Typically, from 10 to 50 mg of energetically hand-milled powder (10 min, mortar/pestle) is directly poured in a three-necked glass vessel containing 40 mL of 0.1 mol/L aqueous solution of H_2O_2 (stock solution: Acros Organics, $d = 1.135$, 35% in water), and the vessel is immediately plugged to a pneumatic airtight system enlisting a water-filed volumetric measuring buret ($\Delta V = 0.1$ mL).[17] This suspension is maintained under vigorous stirring, and the volume of released O_2 is monitored as a function of time (V_t) at constant temperature. When the O_2 evolution stops, the maximum measured volume (i.e., $V_o \approx 58$ mL in our experimental conditions) can be considered as proportional to the initial H_2O_2 concentration in the solution, so that, at any time of reaction, ($V_o - V_t$) is proportional to the remaining H_2O_2 concentration. Blank run experiments performed without powder show that the spontaneous decomposition of the hydrogen peroxide can be neglected (0.5%) in our experimental settings up to a temperature of 40 °C and within the typical duration of the experiments. Other blank experiments additionally show that the light exposure intensity has no influence onto the catalytic performances of the powders, ruling out photocatalytic activity. For the determination of the activation energy, the suspension temperature is controlled by a PID-thermocouple system, and the amount of powder was reduced in order to limit the effect of the exothermicity of the reaction onto the medium temperature. Occasionally, the concentration of the stock H_2O_2 solution was checked by potassium permanganate titration. As the gas trapped in the pneumatic volumetric measuring device is progressively enriched in O_2 while the decomposition reaction proceeds, we checked that its dissolution in the water contained in the measuring buret had no detectable impact on the measure of the gas volume, thanks to the relatively very small surface of the contact meniscus.

Results and Discussion

The X-ray diffraction patterns of the as-prepared nanosized Co_3O_4 material (Co_3O_4-AP) and the powders obtained after annealing of this pristine material at 150, 200, 300, 400, 500, 600, 700, and 800 °C in air are shown in Figure 2. All the diffraction patterns can be indexed with the $Fd\bar{3}m$ space group (ICSD file #28158[14]), although important differences can be noticed. In the diffraction pattern of the pristine material, the peaks are significantly broad, in agreement with the nanometric nature of the sample. Upon annealing, the

(10) Brunauer, S.; Emmet, P. H.; Teller, E. *J. Am. Chem. Soc.* **1938**, *60*, 309.
(11) Barrett, E.; Joyner, L.; Halenda, P. *J. Am. Chem. Soc.* **1951**, *73*, 373.
(12) Rodríguez-Carvajal, J. *Physica B* **1993**, *192*, 55.
(13) Thompson, P.; Cox, D. E.; Hastings, J. B. *J. Appl. Crystallogr.* **1987**, *20*, 79.
(14) Smith, W. L.; Hobson, A. D. *Acta Crystallogr., Sect. B* **1973**, *29*, 362.
(15) Scherrer, P. *Nach. Ges. Wiss. Gott.* **1918**, *2*, 98.
(16) Stokes, A. R.; Wilson, A. J. C. *Proc. Phys. Soc. London* **1944**, *56*, 174.
(17) Kanungo, S. B.; Parida, K. M.; Sant, B. R. *Electrochim. Acta* **1981**, *26* (8), 1157.

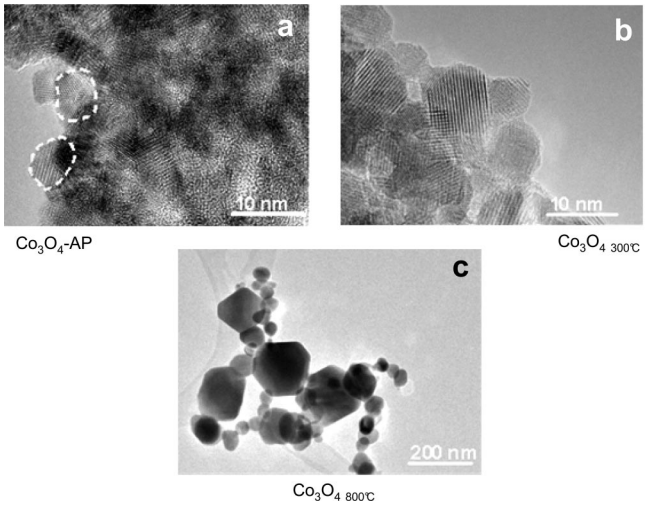

Figure 3. TEM and HRTEM images for (a) Co_3O_4-AP, (b) Co_3O_4 300 °C, and (c) Co_3O_4 800 °C.

peaks become sharper as a result of an increase in crystallite size and the loss of internal microstrains. More surprising here are the strong variations in relative XRD peaks intensities, with mainly the (111)/(220) intensity ratio, which is abnormally high for Co_3O_4-AP, but then progressively decreases with temperature to reach the ratio value expected for an ideal spinel structure. Similar unusually high (111) intensity has been previously observed in precipitated Co_3O_4, although no origin was specified,[18,19] and in Co^{4+} containing $H_{0.6}Li_{0.18}Co_{2.62}O_4$ phase electrochemically prepared from CoO. For the latter, cobalt vacancies in both tetrahedral Td and octahedral Oh sites were found to be at the origin of the abnormal intensity distribution, although the location of Li^+ and H^+ remained unclear.[20,21]

TEM images of Co_3O_4-AP, Co_3O_4 300 °C and Co_3O_4 800 °C samples (Figure 3) show pseudospherical particles and a sharp size distribution for low temperature batches (4 and 8 nm for Co_3O_4-AP and Co_3O_4 300 °C, respectively), whereas large size dispersion is noticed for higher annealing temperatures (20−200 nm for Co_3O_4 800 °C). For low size dispersion samples, the very good agreement between the calculated geometrical surface ($\rho = 6$ g/cm^3) and the values of BET specific surface areas computed from N_2 adsorption (Table 1) suggests that the particles are dense with very low internal porosity. These observations confirm that crystallite size is therefore one major source of peak broadening for the low temperature samples. Despite many observations, we were not able to detect any particles lying on their edge, piling, or with nonisotropic shape, indicating very unlikely anisotropy of the particles as possible origin of the intensity inversion.

Because of these observations, changes in the atomic distribution must be considered in order to explain the particular intensity distribution of our nanometric samples. Two types of defects in spinels should thus be taken into account to explain our data. The first one deals with cation vacancies, which can enlist either cobalt vacancies leading to an oxygen rich spinel or the departure of two ions of opposite charge (Schottky defects). In contrast, the second one involves an interstitial cation (Frenkel defects) displaced from its initial position and leading to a vacancy.

The Co^{2+}/Co^{3+} inversion has not been considered, as these ions have very close diffusion factor in our diffraction conditions.

Our previous work[6] led to the formula $Co_3O_4 \cdot 2.2\ H_2O$ for Co_3O_4-AP on the basis of the mean cobalt oxidation state (2.66 ± 0.03), atomic absorption, TGA, and coupled TGA-mass spectrometry analyses. As the initial mean cobalt oxidation state is maintained upon increasing temperature, we can exclude the possibility of large amounts of vacancies resulting from Schottky defects as being the main origin for the temperature-driven abnormal intensity distribution. In addition, the absence of oxygen release upon heating rules out the possibility of anionic excess.[6] However, the possibility that an invariable low amount of such cobalt vacancies might be present in our materials was still considered. The choice of the vacancy location is, however, not simple, as there might be vacant octahedral sites, tetrahedral sites, or both. The available experimental studies on different spinel type compounds indicate various structural models without reaching a final consensus. As an example, for stoichiometric $MgAl_2O_4$ spinels, all combinations have been proposed [22−24] although a single-crystal study concluded that vacancies never solely exist in tetrahedral sites but are most likely parted between tetrahedral and octahedral sites with a preference for the latter.[25] For hausmanite, a vacancy distribution dependent on the Mn oxidation state has been reported in tetrahedral sites when $Mn^{3+}/Mn^{2+} \leq 2.4$ and in both sites otherwise.[7] Finally, more relevant to the present paper, is either the formation of octahedral vacancies proposed by Angelov et al.[26] in oxygen-rich $Co_{3-x}O_4$ powders as deduced from EPR analysis or the presence of both octahedral and tetrahedral cobalt vacancies in the $H_{0.58}Li_{0.18}Co_{2.53}O_4$ and $H_{0.96}Co_{2.76}O_4$ phases as recently put forward by Tronel et al.[20]

In light of the aforementioned literature, Rietveld refinement of reference Co_3O_4 800 °C sample was thus performed considering all possible combinations (none, octahedral, tetrahedral, and both types of vacancies) and taking the structure of ICSD file #28158 as starting model. Scale factor, zero point, cell dimensions, microstructural parameters, atomic coordinates, atomic occupancies and atomic displacement factors were refined, although the latter were constrained to the same value for both types of cobalt atoms

(18) Furlanetto, G.; Formari, L. *J. Colloid Interface Sci.* **1995**, *170*, 169.
(19) Cao, L.; Lu, M.; Li, H. L. *J. Electrochem. Soc.* **2005**, *152* (5), A871.
(20) Tronel, F.; Guerlou-Demourgues, L.; Menetrier, M.; Croguennec, L.; Goubault, L.; Bernard, P.; Delmas, C. *Chem. Mater.* **2006**, *18*, 5840.
(21) Douin, M.; Guerlou-Demourgues, L.; Ménétrier, M.; Bekaert, E.; Goubault, L.; Bernard, P.; Delmas, C. *Chem. Mater.* **2008**, *20* (21), 6880.
(22) Dupree, R.; Lewis, M. H.; Smith, M. E. *Philos. Mag. Lett.* **1986**, *53* (2), L17.
(23) Kovtunenko, P. V. *Glass Ceram.* **1997**, *54* (7−8), 242.
(24) Ibarra, A.; Vila, R.; Jimenez de Castro, M. *Philos. Mag. Lett.* **1991**, *64* (1), 45.
(25) Sheldon, R. I.; Hartmann, T.; Sickafus, K. E.; Ibarra, A.; Scott, B. L.; Argyriou, D. N.; Larson, A. C.; Vondreele, R. B. *J. Am. Chem. Soc.* **1991**, *82* (12), 3293.
(26) Angelov, S.; Zhecheva, E.; Stoyanova, R.; Atanasov, M. *J. Phys. Chem. Solids* **1990**, *51* (10), 1157.

Table 1. Structural and Textural Characterization for Co_3O_4-AP and Air-Annealed Co_3O_4 $_{T°C}$ Enlisting BET Surface Area Values and Rietveld Refinement Details: *a* Cell Parameter, *u* Anionic Parameter, Atomic Occupations, Crystallite Size (from XRD and BET), Microstrains ($\delta d/d$) × 10^4 and R_p, R_{wp}, R_e and R_B Agreement Factors

sample	BET surface area (m^2/g)	*a* (Å)	*u*	occ. 16d	%Co	occ. 8a	%Co	occ. 48f	%Co	occ. 16c	%Co	crystallite size (Å) from XRD	crystallite size (Å) from BET	strains ($\Delta d/d$) × 10^4	R_p, R_{wp}, R_e, R_B (%)
Co_3O_4-AP	230	8.090(2)	0.2717(5)	1.892(6)	64.03	0.72(5)	24.50	0.153(6)	5.16	0.19(5)	6.31	32	43	57	12.3, 11.2, 7.67, 2.05
$Co_3O_{4\ 150\ °C}$	205	8.089(2)	0.2689(6)	1.90(3)	64.22	0.797(8)	26.98	0.17(3)	5.62	0.094(8)	3.19	41	48	44	9.5, 8.29, 5.01, 1.79
$Co_3O_{4\ 200\ °C}$	182	8.0862(9)	0.2678(3)	1.92(2)	64.89	0.822(7)	27.82	0.13(2)	4.53	0.081(7)	2.76	54	55	46	10.2, 8.25, 5.51, 1.98
$Co_3O_{4\ 300\ °C}$	125	8.089(1)	0.2667(5)	1.93(2)	65.22	0.883(8)	29.87	0.07(2)	2.39	0.075(8)	2.52	78	80	44	10.5, 8.26, 5.11, 1.40,
$Co_3O_{4\ 400\ °C}$	74	8.0854(7)	0.2661(3)	1.939(5)	65.61	0.923(5)	31.24	0.044(5)	1.48	0.049(1)	1.67	102	130	34	11.2, 8.25, 5.4, 1.62
$Co_3O_{4\ 500\ °C}$	36	8.0866(5)	0.2649(5)	1.96(2)	66.17	0.96(1)	32.64	0.02(2)	0.64	0.02(1)	0.55	227	277	14	6.59, 8.20, 2.42, 2.77
$Co_3O_{4\ 600\ °C}$	25	8.083(4)	0.2651(5)	1.956(6)	66.17	0.980(6)	33.17	0.001(6)	0.05	0.018(6)	0.62	1000	400	9	6.86, 8.99, 2.17, 2.61
$Co_3O_{4\ 700\ °C}$	21	8.0831(1)	0.2657(5)	1.956(3)	66.17	0.983(3)	33.27	0	0.01	0.017(3)	0.56	>1000	476	4	8.24, 10.1, 2.26, 2.88
$Co_3O_{4\ 800\ °C}$	1	8.0827(5)	0.2649(4)	1.956(5)	66.17	1	33.83	0	0.00	0	0.00	>1000	900	4	9.54, 11.9, 2.13, 3.46

(8a and 16d sites). Background profile was refined by adjusting the height of preselected points for linear interpolation. Our best fit is shown in Figure 4a and corresponds to the formula $[Co_1]_{tet}[Co_{1.956}\square_{0.044}]_{oct}O_4$, suggesting that a slight nonstoichiometry would be present in our powders due to the presence of an excess of Co^{+III} that would be compensated by octahedral vacancies, in agreement with Angelov et al.[26] Note that this deviation from the ideal octahedral site occupation falls within the range of accuracy of our oxidation state determination. Although the refined amount of vacancies is barely significant, the refined cell parameter seems to confirm their presence as the obtained value (a = 8.0827(5) Å) is somewhat lower than the ideal value (8.084 Å). As the amount of vacancies would remain invariable upon annealing, the same amount was kept in the refinement for the other samples of the series.

The next step was then to attempt the Rietveld refinement of the diffraction pattern of the as-prepared sample, Co_3O_4-AP, with the addition of cobalt interstitial-vacancy pairs, or Frenkel defects. Dieckmann[8] already pointed out that cobalt interstitials and vacancies could be the defect species controlling oxygen activity in Co_3O_4 although no details have been published to date. Similarly, Stoyanova et al. observed the presence of Co^{2+} (d^7) in 48f interstitial sites in a Co_3O_4 spinel doped with lithium[27] by means of EPR, but no quantitative determination of these cobalt interstitials was reported. In this case, the situation is more complex than in the vacancy determination as there is one octahedral site (16c Wyckoff sites) and two types of tetrahedral sites (8b and 48f Wyckoff sites) available in the spinel structure (Figure 1b). As a consequence, each type of interstitial cation can be located on three different interstitial positions, and seven different species (16c interstitials, 8b interstitials, 48f interstitials, 16c+8b interstitials, 16c+48f interstitials, 8b+48f interstitials, 16c+8b+48f interstitials) have to be considered.

To test all possible combinations for the refinement of the Co_3O_4-AP, we constrained the total amount of cobalt atoms in the structure to the value obtained in the refinement of $Co_3O_{4\ 800\ °C}$ (ΣCo = 2.956), and the occupation values of the possible interstitial positions were allowed to increase at the expense of the occupations of the ideal positions. Such assumption is based on the facts that our samples were single phased and did not show the presence of amorphous phase as deduced from XRD and HRTEM, respectively. Profile parameters were also refined in order to model the strong broadening of the diffraction peaks because of the small size of the diffraction domains and the presence of microstrains. The best fit (Figure 4b) was obtained considering the simultaneous presence of interstitial cobalt in both 16c and 48f Wyckoff sites. Although the lack of long-range order due to the small size of the crystallites and to the presence of structural defects might induce inaccuracies in the structural description (indeed, the final fit still has some features that are not perfectly modeled) the obtained results can still give close idea of the average structure. The refinement of all three interstitial positions leads to a negligible occupation of 8b Wyckoff sites (0.3%), which is not a surprise as the cavity in these sites is too small for cobalt atoms (Co_{8b}−O ≈ 1.5 Å). The refinement of the atomic occupation factors finally gives a structure with 6.31 and 5.16% of the total amount of cobalt atoms in 16c and 48f sites, respectively. The corresponding vacancies are mainly found in the 8a sites (27.6% vacant sites) rather than in the 16d sites (5.4% vacant sites). Looking at the local environments of the available spinel positions, one might think that because of electrostatic repulsions, any interstitial 16c atom would come from the neighboring 8a site and that a 48f interstitial would be created for every vacant 16d position. However, our results clearly indicate that the more stable configuration is in fact a distribution of interstitial atoms among both sites. In such scenario, the simultaneous occupation of neighboring sites could be stabilized by two relaxation mechanisms: displacement of cobalt atoms from their ideal positions toward vacant sites and displacement toward the surface, which we believe might play an important role given the high surface/volume ratio of the particles.

Both the refined cell parameter (a = 8.090(2) Å) and the ionic parameter (u = 0.2717(5)) are higher than the ideal

(27) Stoyanova, R.; Zecheva, E.; Angelov, S. *Mater. Chem. Phys.* **1990**, *26*, 239.

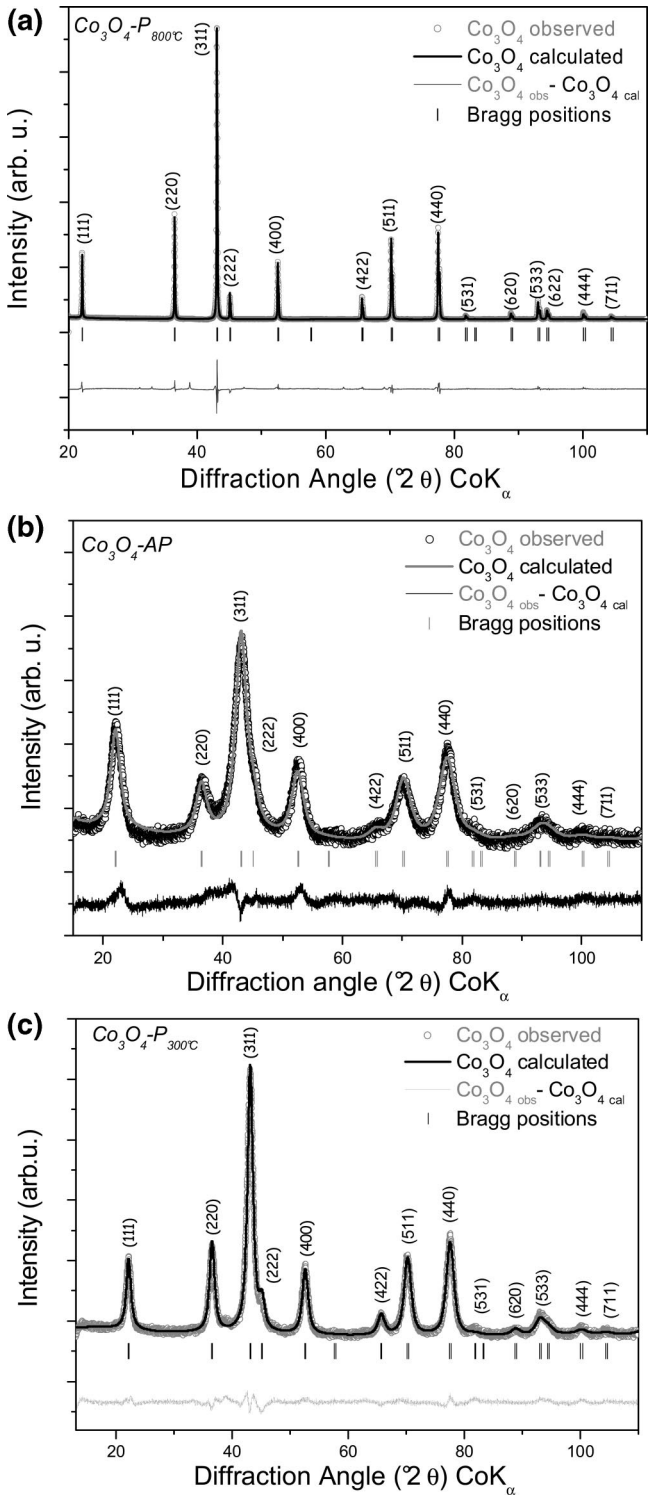

Figure 4. Rietveld refinements for (a) Co_3O_4 $_{800\ °C}$, (b) Co_3O_4-AP, and (c) Co_3O_4 $_{300\ °C}$. For each sample, the experimental X-ray powder diffraction pattern (dotted curve) is compared with the Rietveld-refined profile (solid line). The Bragg peaks positions and the difference curves are shown as well.

values, indicating a loss of compactness in the atomic arrangement in agreement with the existence of Frenkel defects[28] and surface relaxation effects. A mean crystallite diameter of 32 Å is obtained, in good agreement with TEM and BET measurements (Table 1). Microstrains are also found in our pristine material, as indicated by a $\Delta d/d$ value of 57×10^{-4}, which indicates that the cell parameter suffers from fluctuations due to the presence of these defects.

Once the origin of the abnormal intensity distribution was identified for Co_3O_4-AP, the diffraction patterns of the heated Co_3O_4 $_{T°C}$ samples (e.g., Co_3O_4 $_{300\ °C}$, Figure 4c) were refined in order to follow the evolution of the structural defects during the process. Each diffraction pattern was refined taking as initial structural parameters those obtained for the previous temperature. For example, the parameters obtained for Co_3O_4-AP were used as starting values for Co_3O_4 $_{150\ °C}$. To mimic the diffusion processes occurring upon annealing, we considered that migration can occur only via face-sharing polyhedra, so the atomic occupations were carefully refined using constraints between neighboring sites. For example, taking into account that interstitial 16c octahedra only share faces with 8a and 48f tetrahedral sites (Figure 5a), only atomic transfers from 16c to 8a and 48f sites were allowed. Similarly, the occupations of 48f sites were constrained with those of the face-sharing 16c and 16d octahedral sites. The transfer between interstitial 16c and 48f positions was allowed because according to the initial distribution of interstitials and vacancies, the ionic distribution of the final compound can be reached only if this exchange is considered. Following this strategy, we could refine all the diffraction patterns for the Co_3O_4 $_{T°C}$ samples; the results are shown in Table 1 and plotted in Figure 6 as a function of the annealing set temperature.

From these results, a clear decrease in the amount of interstitial 16c+48f atoms is observed upon annealing to the benefit of the ideal 16d and 8a positions, as expected from the evolution in the intensities of the X-ray diffraction peaks. Interestingly, the amount of interstitial 16c cobalt atoms initially decreases much faster than the amount of interstitial 48f atoms. To explain this, the number and type of first neighbors for each interstitial site should be analyzed. As a 16c octahedron shares 6 faces with 48f tetrahedra and 2 faces with 8a tetrahedra (Figure 5b), the diffusion of a 16c interstitial atom through a 48f site will be statistically more probable (and enhanced by the initial filling level as the 48f are almost empty but 8a are 2/3 filled), but the migration through an ideal 8a site will be thermodynamically favored. On the other hand, each 48f tetrahedron shares 2 faces with 16c and 2 faces with 16d positions (Figure 5c), thus interstitial 48f atoms can diffuse toward both octahedral sites with the same probability, but 16d sites will be thermodynamically favored. According to this scenario, in the first stage of the annealing process, a large amount of 16c interstitial atoms will diffuse toward 48f and 8a positions. Although the latter are now lying in stable positions, the former will then migrate to stable 16d sites, the 48f positions being continuously refilled with cations transiting from 16c to 16d sites. The 8a positions are filled quicker than 16d simply because more sites are available as the initial amount of vacancies in 8a sites is higher.

It is worth mentioning that these results, which provide important insights regarding the origin of the temperature-

(28) Quéré, Y. *Défauts ponctuels dans les métaux*; Masson et Cie: Paris, 1967.

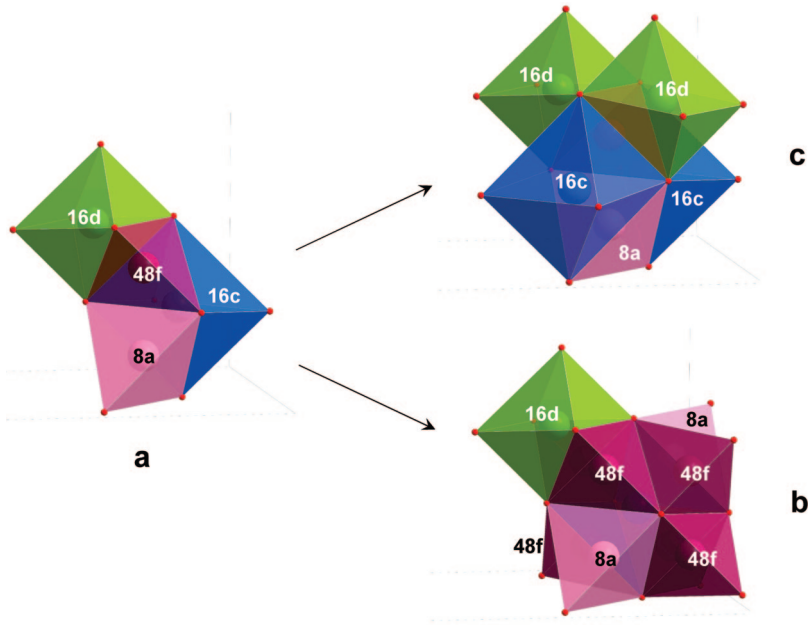

Figure 5. Graphic representation of the geometric environment of (b) 16c and (c) 48f interstitial positions in the spinel structure (a).

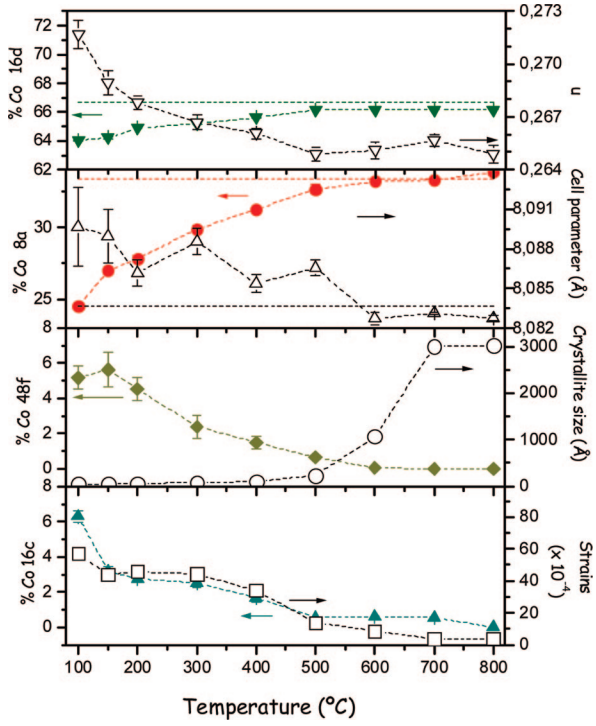

Figure 6. Evolution, as a function of the annealing temperature, of the %Co in the different crystallographic sites, *u* anionic parameter, a cell parameter, crystallite size and amount of strains deduced from the Rietveld refinements. Discontinuous lines indicate ideal values.

driven decrease in interstitial defects, are also consistent with the decrease in the anionic parameter *u*, cell parameter, and amount of microstrains with increasing temperature.

Turning now to the mosaic nature of the particles, an interesting question regards the influence of the grain boundaries on their reactivity (e.g., catalyst activity). From Co_3O_4-AP to Co_3O_4 $_{500\ °C}$, a very good agreement between the crystallites size refined from the XRD Bragg peaks width and the crystallites size calculated from the BET surface area

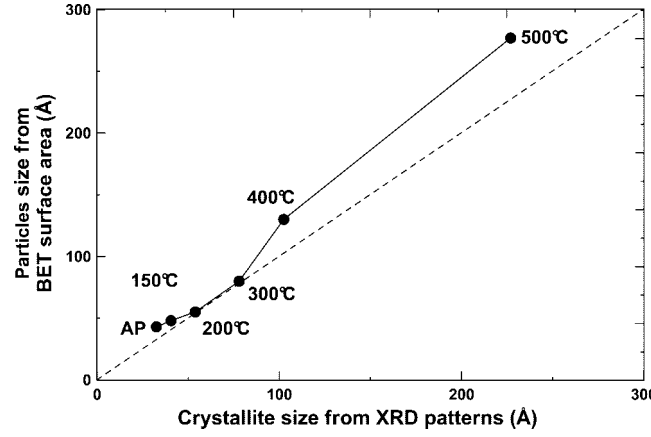

Figure 7. Comparison of the crystallites size calculated from the BET surface area values and refined from the XRD patterns, for pristine Co_3O_4-AP and Co_3O_4 $_{T°C}$ with $T \leq 500$ °C. The dash line represents the ideal evolution for perfectly monolithic samples.

values (Table 1, Figure 7) unambiguously demonstrates that these samples are mostly made of monolithic particles, as also observed by HRTEM. Above 500 °C, the crystallites size sharply increases but the values from XRD strongly deviate from those from BET data, indicating the formation of mosaic texture.

All the above results demonstrate that these samples, ranging from Co_3O_4-AP to Co_3O_4 $_{800\ °C}$, have evolving structural and textural parameters while maintaining a constant Co/O stoichiometry. Because the low-temperature samples have very high specific surface areas and are monolithic, they constitute a model system to test the sole effect of the surface defects and strains onto surface reactivity, namely catalytic properties, without any need of cationic substitution (i.e., change in chemical composition) as often reported in the literature.

Among the numerous catalytic reactions available, we decided to focus on the decomposition of diluted hydrogen peroxide aqueous solutions; it requires a simple experimental

setup to be monitored and for which there is also a wealthy literature; the mean reason being to grasp further insight into the destabilization of the peroxide species, which is a cornerstone in view of finding more efficient catalysts for Li/O_2 batteries, presently governed by empiric rules.

The catalytic characterization of our samples was carried out as follows. First, we determined the order of the H_2O_2 decomposition reaction using the initial rate method; second, we calculated the activation energy, and third the rate constants $k_{20\ °C}$ ($s^{-1}\ m^{-2}$) for the pristine Co_3O_4-AP and some annealed $Co_3O_{4\ T°C}$ samples.

Because our pristine and low-temperature annealed samples are made of micrometric porous agglomerates of nanosized Co_3O_4 domains leading to finely distributed nanoporosity,[6] limited diffusion of inward reactants and outward products was experienced. Through additional preliminary trials, the measured catalytic activity was found to be highly dependent on the weight of powder over the volume of solution, on the preparation of the powder (e.g., grinding or not) and on the way the tests were performed (e.g., stirring or not). We independently modified our experimental parameters in order to eschew the aforementioned issues and reach our final test protocol. Low diffusion effect was finally reached by using (1) small amounts of powder (10 mg for 40 mL of solution), (2) constant and strong stirring of the suspension, and (3) thoroughly hand-milled samples (10 min). This last point does not come as a surprise because we have previously shown[6] that this milling treatment not only considerably reduces the internal interparticles nanoporosity of the agglomerates by breaking them into smaller ones but also creates much larger interagglomerate pores whose surfaces are more easily accessible to reacting species. Additionally, we believe that the intense gas release during the early stage of the H_2O_2 decomposition triggers the fracture of the agglomerates into individual particles or at least smaller agglomerates, as deduced from the not decanting suspension recovered once the reaction is over in opposition to the fast settling powder observed in H_2O_2-free distilled water.

Under these experimental conditions, we measured the initial rate constants ($t \approx 0$) for various initial H_2O_2 concentrations, leading us to a true *order* (i.e., order with respect to concentration $= n_c$) of reaction nearly equal to one ($p = 0.93$), in agreement with previous reports.[29] Because the products of the decomposition reaction are both the solvent itself (H_2O) and very slightly soluble O_2 molecules, it is very unlikely that the order with respect to concentration is drastically different from the order with respect to time (n_t). This first-order was confirmed by the linear evolution of $\mathrm{Log}(V_o/(V_o - V_t))$ as a function of time, as exemplified in Figure 8 for Co_3O_4-AP and $Co_3O_{4\ 400\ °C}$, allowing us to easily calculate the rate constants k_T. From k_T values of the Co_3O_4-AP sample recorded at various temperatures from 20 to 40 °C, the E_a activation energy was found to be equal to 60 ± 5 kJ/mol (Figure 9), in good agreement with previously reported values for micrometric and high temperature prepared Co_3O_4 samples.[30−32] At first sight, these results

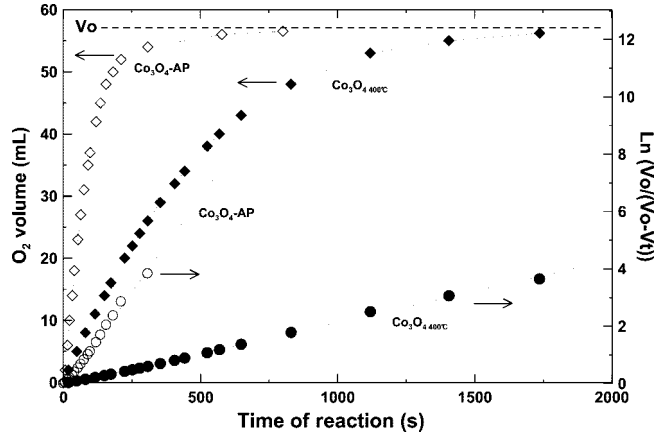

Figure 8. Evolution in volume of produced O_2 ($H_2O_2 \rightarrow H_2O + 1/2\ O_2$) and of Log(Vo/(Vo-Vt)) as a function of the reaction time. Volumes are measured at constant temperature (20 °C) and constant atmospheric pressure; and Vo corresponds to the volume of O_2 measured at t_∞. For sake of clarity, data are only shown for Co_3O_4-AP and $Co_{3}O_{4\ 400\ °C}$.

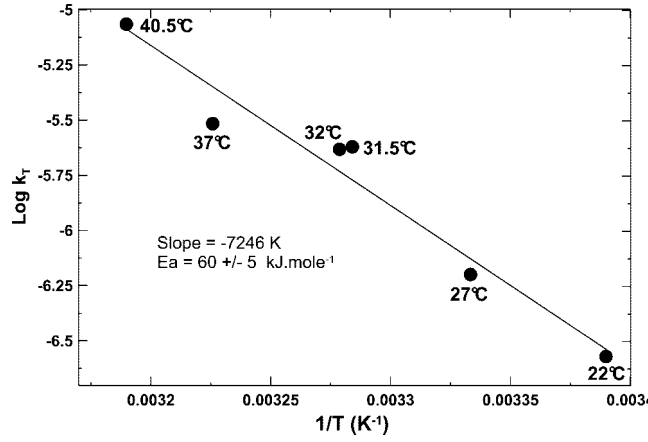

Figure 9. Arrhenius $\mathrm{Log}(k_T) = f(1/T)$ plot for the reaction decomposition of H_2O_2 aqueous solutions in contact with Co_3O_4-AP sample. Volumes of released O_2 are measured at constant temperatures and constant atmospheric pressure. Related slope and E_a activation energy values are also given.

suggest that the catalytic activity of the faulted Co_3O_4-AP material is not drastically different from that of the ideal spinel materials. However, the E_a value is ruling the evolution of the rate constant with respect to temperature, but not the absolute intrinsic constant values which are reported to depend on numerous parameters. Figure 10 depicts the evolution of the $k_{20\ °C}$ ($s^{-1}m^{-2}$) rate constants as a function of the total proportion of structural defects and strains, from Co_3O_4-AP to $Co_{3}O_{4\ 500\ °C}$ samples and for $Co_{3}O_{4\ 800\ °C}$ as a defect-free reference sample. Thanks to their above-mentioned monolithic nature, the choice of the samples heated at temperatures lower to 600 °C enables us to discard any grain-boundaries catalytic effect. Figure 10a, shows a clear relationship between the rate constant and the total amount of structural defects in our samples, with the highest rate constant having the highest amount of defects. From Figure 10b, the proportionality with the microstrains is less straight but a trend can be observed too; the higher the amount of strains, the higher the specific rate constant. This can be derived from the fact that the samples with a larger

(29) Ahuya, L. D.; Brar, A. S. *J. Colloid Interface Sci.* **1975**, *50* (2), 197.
(30) Hernán, L.; Morales, J.; Tirado, J. L. *J. Colloid Interface Sci.* **1986**, *110* (1), 172.
(31) Nasrallah, M. *Mater. Lett.* **2003**, *57*, 914.
(32) Goldstein, J. R.; Tseung, A. C. C. *J. Catal.* **1974**, *32*, 452.

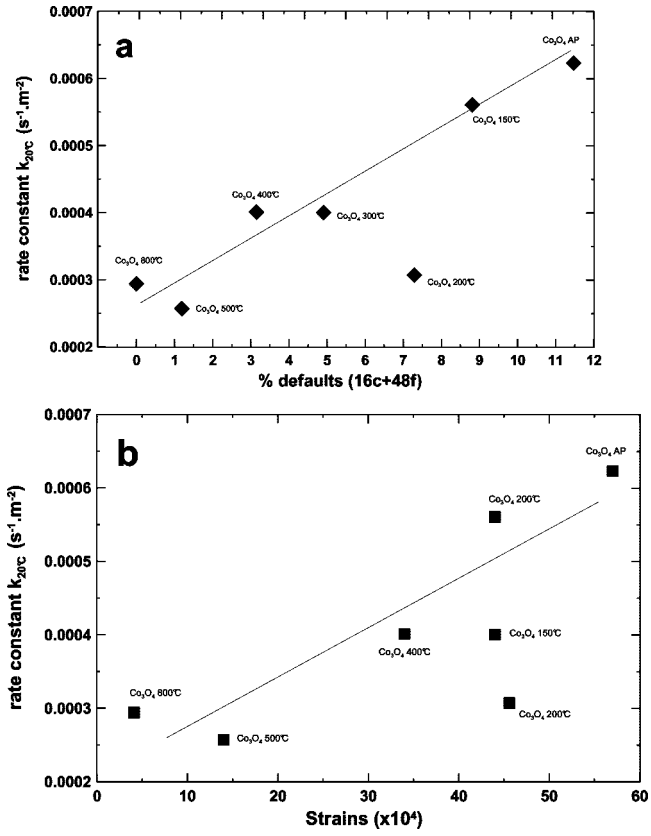

Figure 10. (a) k_T rate constant vs defect amount, and (b) k_T rate constant vs strain amount. Rate constant values (s^{-1} m^{-2}) are related to the hydrogen peroxide decomposition for Co_3O_4-AP and annealed Co_3O_4 $_{T°C}$ ($T \leq 500$ °C) and for Co_3O_4 $_{300\ °C}$ as a defect-free sample.

amount of strains are those with more interstitial defects. For some reason not yet totally understood, the Co_3O_4 $_{200\ °C}$ sample seems to deviate from these trends.

Keeping in mind that our XRD refinements is not enabling us to quantify the specific localization and proportion of Co^{2+} and Co^{3+} in each of the interstitial sites, it is reasonable to believe that this aspect would be worth being later scrutinizing (e.g., by EELS, Raman, or XANES spectroscopic means) in order to provide an additional adjustment parameter for a more accurate rationalization of the catalytic activity of our samples.

These results are expected to have a strong impact within the field of energy storage because of the present renewed interest in Li−O_2 batteries for which there is a growing yet unmet demand for better catalysts for the lithium peroxide decomposition. Because of the similarity between the hydrogen peroxide and lithium peroxide decompositions, one could naively expect that our increased knowledge about H_2O_2 decomposition can also be profitable to the Li_2O_2 one. We are well aware that the spontaneous catalytic decomposition of H_2O_2 aqueous solutions is not fully mimicking the Li_2O_2 oxidation, which is a nonspontaneous electrochemical-driven process, but preliminary results obtained with Co_3O_4-AP in terms of polarization seem to confirm our expectations, and we are now successfully using this test as a qualitative and quantitative fast screening tool for selecting the best catalyst candidates for Li−O_2 cells.

Conclusions

This study has provided further original insights into the defect structure and catalytic activity of nanometric and stoichiometric Co_3O_4 powders obtained by direct precipitation. In addition to the localization and quantification of the interstitial defects, the migration path of the cobalt ions upon annealing was rationalized and better understood thanks to the structural refinements of heated samples. By carefully selecting the samples containing monolithic powders, we here possess a very unique and useful model sample to study the existence of a feasible structural-catalytic activity relationship. As a first attempt, the rate constant for the decomposition of diluted aqueous solutions of hydrogen peroxide at 20 °C was found to be directly proportional to both the amounts of structural interstitial defects and microstrains. The higher the strains level or the defects proportions, the higher the rate constant. In contrast, both the order of reaction and the activation energy are found to be similar regardless of the samples elaboration temperature, particle size, and defect contents. Given the present active search aimed at finding the most efficient catalyst for Li/O_2 cells (i.e., destabilization of Li_2O_2 upon charge), these results related to the decomposition of the peroxide ion enlighten the possibility of using the herein described technique as a very useful strategy to quickly select the most promising catalysts. Needless to say, this way of studying/screening is not limited to cobalt oxides but is now applied to many other compounds.

Acknowledgment. The authors are grateful to P. Bruce (St. Andrews' School of Chemistry), J. Rodriguez-Carvajal (ILL), C. Masquelier (LRCS) and J.-N. Chotard (LRCS) for helpful discussions; to L. Laffont-Dantras (LRCS) for the HRTEM images; and to M. Nelson (LRCS) for her help in reading and correcting this paper.

CM900328G